Generalized Nonequilibrium Fermi's Golden Rule and Its Semiclassical Approximations for Electronic Transitions between Multiple States

Xiang Sun,[*,†,‡,¶,§] Xiaofang Zhang,[†,‡,¶] and Zengkui Liu[†,‡,¶]

†*Division of Arts and Sciences, NYU Shanghai, 567 West Yangsi Road, Shanghai 200124, China*

‡*NYU-ECNU Center for Computational Chemistry at NYU Shanghai, 3663 Zhongshan Road North, Shanghai 200062, China*

¶*Department of Chemistry, New York University, New York, New York 10003, United States*

§*Shanghai Frontiers Science Center of Artificial Intelligence and Deep Learning, NYU Shanghai, 567 West Yangsi Road, Shanghai, 200124, China*

E-mail: xiang.sun@nyu.edu

Abstract

Nonequilibrium Fermi's golden rule (NE-FGR) approach is developed to simulate the electronic transitions between multiple excited states in complex condensed-phase systems described by the recently proposed multi-state harmonic (MSH) model Hamiltonian. The MSH models were constructed for faithfully capturing the photoinduced charge transfer dynamics in a prototypical organic photovoltaic carotenoid-porphyrin-C_{60} molecular triad dissolved in tetrahydrofuran. A general expression of the fully quantum-mechanical NE-FGR rate coefficients for transitions between all pairs of states in the MSH model is obtained with the path-integral formalism. Besides, the linearized semiclassical NE-FGR formula and a series of semiclassical approximations featuring Wigner and classical nuclear sampling choices and different dynamics during the quantum coherence period for the MSH model are derived. The

current approach enables all the possible population transfer pathways between the excited states of the triad, in contrast to the previous applications that only addressed donor-to-acceptor transition. Our simulations for two triad conformations serve as a demonstration for benchmarking different NE-FGR approximations and show that the difference between all levels of approximation is small for the current system, especially at room temperature. By comparing with nonadiabatic semiclassical dynamics, we observe similar timescales of the electronic population transfer predicted by NE-FGR. It is believed that the general formulation of NE-FGR for the MSH Hamiltonian enables a variety of applications in realistic systems.

1 Introduction

Electronic transitions occur in many fundamental processes such as charge transfer (CT) in oxidation-reduction and photochemical reactions in solutions, photovoltaic solar cells, as well as excitation energy transfer (EET) in photosynthetic light-harvesting complexes.[1–15] Routine calculations based on the Born-Oppenheimer approximation such as molecular dynamics (MD) simulations and ground-state electronic structure calculations could not treat this type of problem due to its nonadiabatic nature, i.e., the motions of the electrons and the nuclei cannot be separated. Therefore, computational methods for modeling electronic transition between multiple electronic states are necessary.[16–18]

The most crucial feature of such electronic transitions in the nonadiabatic regime with weak interstate couplings is arguably the kinetic rate constant for transitions between electronic states, which may be described by the equilibrium Fermi's golden rule (FGR).[19,20] The FGR theory describes the rate constant for electronic transition between the donor (initial) and the acceptor (final) electronic states on the level of the second-order time-dependent perturbation theory of quantum mechanics and assumes that the system starts out at the thermal equilibrium with respect to the potential energy surface (PES) of the initial electronic state. The FGR rate theory has been applied in many gas-phase molecular applications, where vibronic eigenstates can be obtained.[21–24] Recently, Heller and Richardson developed the instanton formula for the FGR rate

constant.[25] Saller *et al.* proposed cavity-modified FGR expressions for CT in the optical cavity.[26] Liu *et al.* proposed an imaginary-time open-chain path integral approach for calculating FGR rate constant and demonstrated it in a spin-boson model.[27] For complex condensed-phase systems, however, obtaining the eigenstates of nuclear Hamiltonian is difficult. In order to address this issue for condensed-phase systems, Sun and Geva proposed six levels of semiclassical approximations based on the linearized semiclassical (LSC) approach and highlighted that the classical limit of the LSC FGR formula reduces to the famous Marcus theory[28–31] when assuming no nuclear dynamics and Gaussian statistics of the donor-to-acceptor energy gap.[32] The semiclassical theories of FGR provide practical approaches for studying CT processes in complex and disordered condensed-phase systems, which are described by general anharmonic all-atom force fields for different electronic states. The semiclassical CT rate constant calculation was demonstrated in a prototypical organic photovoltaic carotenoid-porphyrin-C_{60} (CPC_{60}) molecular triad dissolved in explicit tetrahydrofuran (THF) solvent,[33] and interfacial CT in subphthalocyanine (SubPC)/C_{60}[34] and tetraphenyldibenzoperiflanthene (DBP)/C_{70} systems.[35] Recently, an open-source software package CTRAMER for CT rate constant calculation in complex systems was developed.[36]

In the case of photoinduced CT processes, however, the CT molecular system is typically equilibrated on the ground state before the photoexcitation. Upon the sudden vertical excitation that brings the system to a bright locally excited (LE) state or the donor state, the CT molecule and the surrounding solvent are no longer in a stable structural arrangement, thereby inducing a nonequilibrium nuclear relaxation. This nonequilibrium effect of nuclear DOF needs to be accounted for if the timescale of the nuclear structural relaxation for attaining thermal equilibrium on the donor surface is longer than the time scale of the donor-to-acceptor electronic transition. Additionally, because there is not an unambiguous common initial nuclear state in the case of electronic transition between more than two excited states, the equilibrium assumption for the initial nuclear state is no longer satisfied.

To this end, nonequilibrium Fermi's golden rule (NE-FGR) was proposed by Coalson, *et al.*,[37–39] which is designed to address the nonequilibrium nature of the initial nuclear state and

demonstrated in the spin-boson model for two-level systems. The most apparent feature of NE-FGR from FGR is that the electronic transition rate is now a time-dependent rate coefficient in NE-FGR, which is essential for describing photoinduced CT.[40] In the past decade, many developments of NE-FGR have been reported. For example, Izmaylov, *et al.* applied NE-FGR to electronic transition through conical intersections in gas-phase molecules.[41,42] Matyushov developed a theory for radiationless transition rates with nonequilibrium vibrational modes.[43] Borrelli and Peluso developed a second-order cumulant approach that is equivalent to NE-FGR for a two-level molecular system described by normal modes with Duschinsky rotations.[44] Song and Shi compared NE-FGR with numerically exact hierarchical equations of motion for a proton coupled electron transfer reaction.[45] Sun and Geva developed the LSC formulation of NE-FGR for nonequilibrium electronic transition in two-state harmonic models such as the spin-boson model with Condon interstate couplings and the linear vibronic coupling model with non-Condon interstate couplings and proposed a hierarchy of approximations for NE-FGR for both Condon and non-Condon cases.[46,47] Recently, Hu, *et al.* have extended the NE-FGR to atomistic simulations and discovered that the nonequilibrium relaxation in some cases could lead to significant initial enhancement in the NE-FGR rate coefficient from the FGR rate constant even on the instantaneous Marcus theory (IMT) level, which fundamentally alters our understanding of the photoinduced CT process in the condensed phase.[48,49]

However, in the previous applications of NE-FGR, electronic transitions between multiple states were not systematically studied either on the multi-state model level or on the all-atom level. Part of the reason is the lack of a general strategy for constructing effective models for multi-state molecular systems in the condensed phase. Recently, we proposed a consistent approach for mapping the anharmonic all-atom Hamiltonian onto an effective multi-state harmonic (MSH) model Hamiltonian[50,51] and demonstrated that the resulting MSH model can accurately capture the nonadiabatic dynamics compared with all-atom nonadiabatic dynamical simulations of photoinduced CT in the condensed phase.[52]

The MSH model has a globally shared bath and the electronic-nuclear couplings between each

pair of states are built to satisfy the corresponding reorganization energies obtained from MD simulations. For an F-state system, there are total $C_F^2 = F(F-1)/2$ different pairs of states leading to $F(F-1)/2$ reorganization energies restrictions. As pointed out in the previous work, each reorganization energy is related to the equilibrium position shift between the corresponding pair of states.[51] These reorganization energies are probably distinct in a heterogeneous molecular environment, which is very common even in isotropic liquid solutions since the heterogeneity could also arise from the physical nature of different electronic states. For example, molecules in LE and CT states would interact with the environment differently. To have a consistent description of the heterogeneous environment for the multiple electronic states, which can be for the same molecule or for different molecules, we proposed to extend the dimensionality of each normal mode such that the equilibrium positions of all electronic states are represented by a polyhedron in $(F-1)$-dimensional space.[51] The MSH model not only describes the widely-seen correlated and heterogeneous environment such as chromophores with different orientations and intermolecular distances in the Fenna-Matthews-Olson photosynthetic complex,[53] but it can also reduce to the homogeneous limit. Consider the case with a homogeneous environment, if all electronic states couple to the bath equally, the reorganization energies of all pairs of states will be the same and the resulting electronic-nuclear coupling parameters will be reflected by an $(F-1)$-dimensional equilateral polyhedron. Therefore, the MSH model offers a unified approach to construct an effective Hamiltonian for molecules in a heterogeneous or homogeneous environment, which is built to be consistent with all-atom simulations.

In this work, we present a generalized NE-FGR implementation for the MSH model. The current approach will provide a general expression for the fully quantum-mechanical NE-FGR rate coefficient of arbitrary pair of states in the MSH model, which is obtained with exact real-time path-integral formalism. The current approach will address the backward reaction issue, which was neglected in previous NE-FGR applications where only electronic transitions between two states were concerned,[48] and simulate all the possible electronic transitions simultaneously by enabling the electronic transition pathways between all pairs of states in the MSH model.

Moreover, we intend to develop a series of semiclassical approximations for the realistic multi-state systems and compare the performance between quantum-mechanical NE-FGR and its semiclassical approximations using the MSH model.

In specific, we consider the MSH models for the prototypical photoinduced CT system consisting of a CPC_{60} molecular triad dissolved in explicit THF solvent.[54–60] This molecular triad has a wide range of applications including organic photovoltaics, artificial light harvesting, quantum teleportation, molecular wires, and so forth.[54–56,61–63] The donor-bridge-acceptor arrangement of the triad makes it a great candidate for understanding photoinduced CT dynamics: the triad was initially prepared on the ground (G) state, CPC_{60}, which is in thermal equilibrium with the solvent, then abruptly gets photoexcited to the porphyrin-localized excited $\pi\pi^*$ state, CP^*C_{60}. Following the photoexcitation, nuclear relaxation begins while there is some probability for electronic transition to a partially charge-separated state, $CP^+C_{60}^-$, which is referred to as CT1, as well as a fully charge-separated state, $C^+PC_{60}^-$, which is referred to as CT2. We previously investigated the two separate pathways using NE-FGR, i.e., either $CPC_{60}(G) \xrightarrow{h\nu} CP^*C_{60}(\pi\pi^*) \rightarrow CP^+C_{60}^-(CT1)$ or $CPC_{60}(G) \xrightarrow{h\nu} CP^*C_{60}(\pi\pi^*) \rightarrow C^+PC_{60}^-(CT2)$, but the electronic transition between CT1 and CT2 was not allowed.[48] It was discovered that the CT rate constants vary significantly with the triad conformations spanning several orders of magnitude and the solvent motion is playing a big role in CT dynamics.[48,64] Our previous all-atom LSC NE-FGR calculation and its classical limit using IMT for the first pathway show that the triad has a significant nonequilibrium effect from the nuclear initial state, which causes an enhanced CT rate coefficient that is about 40 times larger than the plateau value or the CT rate constant using equilibrium FGR.[48] However, the previous NE-FGR calculation was only applied to a certain donor-to-acceptor transition, given a nonequilibrium initial nuclear sampling, so with two-state NE-FGR we still do not have a comprehensive picture of the entire photoinduced CT process involving electronic transitions between multiple states. The current generalized NE-FGR described above could provide more information regarding the population transfer dynamics in the triad.

The remainder of this paper is organized as follows. Sec. 2 outlines the generalized NE-FGR

formulation for multiple states and its semiclassical approximations. Sec. 3 presents the MSH model Hamiltonian for the photoinduced CT phenomenon of the carotenoid-porphyrin-C_{60} triad dissolved in explicit solvent and provides the NE-FGR expressions for the MSH model at different semiclassical approximation levels. Sec. 4 presents the results and discussion. Sec. 5 provides the concluding remarks.

2 Theory

2.1 Nonequilibrium Fermi's Golden Rule

We start with briefly reviewing the NE-FGR for two-state Hamiltonian

$$\hat{H} = \hat{H}_0 + \hat{H}_I = \begin{pmatrix} \hat{H}_D & \hat{V}_{DA} \\ \hat{V}_{AD} & \hat{H}_A \end{pmatrix}, \tag{1}$$

which is composed of the zeroth-order Hamiltonian, $\hat{H}_0 = \hat{H}_D|D\rangle\langle D| + \hat{H}_A|A\rangle\langle A|$, and the perturbation, $\hat{H}_I = \hat{V}_{DA}|D\rangle\langle A| + \hat{V}_{AD}|A\rangle\langle D|$. Here, the D and A denote the donor and acceptor electronic states, respectively, and the corresponding nuclear Hamiltonians are given by

$$\hat{H}_{D/A} = \frac{\hat{\mathbf{P}}^2}{2} + V_{D/A}(\hat{\mathbf{R}}), \tag{2}$$

where $\hat{\mathbf{R}} = \left(\hat{R}_1, \ldots, \hat{R}_{N_n}\right)$ and $\hat{\mathbf{P}} = \left(\hat{P}_1, \ldots, \hat{P}_{N_n}\right)$ are the mass-weighted nuclear positions and momenta and the nuclear DOF is N_n. The interstate couplings are assumed as constant under the Condon approximation, such that $\hat{V}_{DA} = \hat{V}_{AD} = \Gamma_{DA} = \text{Const.}$

If the initial nuclear state is described by an arbitrary density operator $\hat{\rho}(0)$ and the initial electronic state is $|D\rangle\langle D|$, then the donor population at a later time t is

$$P_D(t) = \text{Tr}_N \text{Tr}_e \left[e^{-i\hat{H}t} |D\rangle\hat{\rho}(0)\langle D| e^{i\hat{H}t} \right], \tag{3}$$

where $\mathrm{Tr}_N\mathrm{Tr}_e[\cdot]$ denotes the trace over the nuclear and the electronic Hilbert spaces.

NE-FGR treats the interstate electronic coupling term as a small perturbation on the second-order time-dependent perturbation theoretical level. If one further assumes that the backward reaction of $A \to D$ is negligible, NE-FGR provides the following approximation expression for the donor-state population:[37]

$$P_D(t) = 1 - \int_0^t \mathrm{d}t' k_{D\to A}(t') + \cdots \approx \exp\left[-\int_0^t \mathrm{d}t' k_{D\to A}(t')\right], \tag{4}$$

where the time-dependent rate coefficient for reaction $D \to A$ is given by

$$\begin{aligned} k_{D\to A}(t) &= \frac{2}{\hbar^2}\mathrm{Re}\int_0^t \mathrm{d}t'\ \mathrm{Tr}_N\left[\hat{\rho}(t)\hat{V}_{DA}e^{-i\hat{H}_A t'/\hbar}\hat{V}_{AD}e^{i\hat{H}_D t'/\hbar}\right] \\ &= \frac{2}{\hbar^2}\mathrm{Re}\int_0^t \mathrm{d}t'\ \mathrm{Tr}_N\left[\hat{\rho}(0)\left(e^{i\hat{H}_D t/\hbar}\hat{V}_{DA}e^{-i\hat{H}_A t/\hbar}\right)\right. \\ &\quad \left.\times\left(e^{i\hat{H}_A(t-t')/\hbar}\hat{V}_{AD}e^{-i\hat{H}_D(t-t')/\hbar}\right)\right] \\ &= \frac{2}{\hbar^2}\mathrm{Re}\int_0^t \mathrm{d}\tau\ \mathrm{Tr}_N\left[\hat{\rho}(0)\tilde{V}_{DA}(t)\tilde{V}_{AD}(\tau)\right] \\ &= \frac{2}{\hbar^2}\mathrm{Re}\int_0^t \mathrm{d}\tau\ C_{DA,AD}(t,\tau). \end{aligned} \tag{5}$$

Here, the nuclear density operator $\hat{\rho}(t)$ is obtained by evolving for time t on the donor PES starting from $\hat{\rho}(0)$,

$$\hat{\rho}(t) = e^{-i\hat{H}_D t/\hbar}\hat{\rho}(0)e^{i\hat{H}_D t/\hbar}, \tag{6}$$

and the time variable to $\tau = t - t'$. We denote

$$\tilde{V}_{jk}(t) \equiv e^{i\hat{H}_j t/\hbar}\hat{V}_{jk}e^{-i\hat{H}_k t/\hbar}, \quad (j \neq k), \tag{7}$$

and $\langle\cdot\rangle = \mathrm{Tr}_N[\hat{\rho}(0)\cdot]$, so that the time correlation function (TCF) can be written as[65]

$$C_{DA,AD}(t,\tau) = \left\langle \tilde{V}_{DA}(t)\tilde{V}_{AD}(\tau)\right\rangle. \tag{8}$$

Next, we consider the general F-state Hamiltonian given by

$$\hat{H} = \begin{pmatrix} \hat{H}_1 & \hat{V}_{12} & \cdots & \hat{V}_{1F} \\ \hat{V}_{21} & \hat{H}_2 & \cdots & \hat{V}_{2F} \\ \vdots & \vdots & \ddots & \vdots \\ \hat{V}_{F1} & \hat{V}_{F2} & \cdots & \hat{H}_F \end{pmatrix}, \tag{9}$$

where the interstate couplings are assumed to be constants, i.e., $\hat{V}_{jk} = \hat{V}_{kj} = \Gamma_{jk}$ in the Condon case, and the nuclear Hamiltonian of the j-th electronic state is

$$\hat{H}_j = \frac{\hat{\mathbf{P}}^2}{2} + V_j(\hat{\mathbf{R}}), \quad (j = 1,\ldots,F). \tag{10}$$

Instead of assuming no backward reaction and only considering the $D \to A$ reaction, we consider all possible reaction pathways in this multi-state system. The equations of motion for the electronic population can be written in the form of Pauli's master equations as below[19,20]

$$\frac{\mathrm{d}}{\mathrm{d}t}P_k(t) = \sum_{j\neq k} k_{j\to k}(t)P_j(t) - \sum_{j\neq k} k_{k\to j}(t)P_k(t), \quad (j = 1,\ldots,F), \tag{11}$$

where the NE-FGR time-dependent rate coefficient $k_{j\to k}(t)$ for pathway $j \to k$ is defined as

$$k_{j\to k}(t) = \frac{2}{\hbar^2}\mathrm{Re}\int_0^t \mathrm{d}\tau\, C_{jk,kj}(t,\tau), \quad (j,k = 1,\ldots,F), \tag{12}$$

$$C_{jk,kj}(t,\tau) = \left\langle \tilde{V}_{jk}(t)\tilde{V}_{kj}(\tau)\right\rangle. \tag{13}$$

The F-coupled differential equations in Eq. 11 have to be solved simultaneously, which involves all possible reaction pathways $j \to k$ and $k \to j$ for any $j \neq k$.

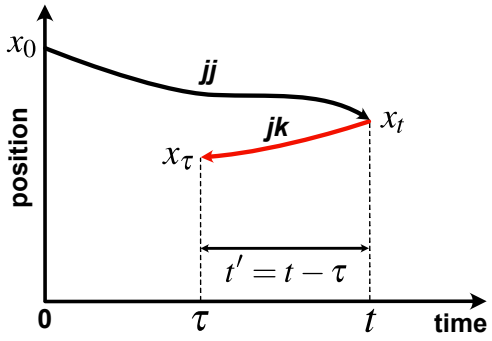

Figure 1: Schematic representation of quantum time correlation function $C_{jk,kj}(t,\tau) = \left\langle \tilde{V}_{jk}(t)\tilde{V}_{kj}(\tau)\right\rangle$, where the first forward propagation is under an electronic population $|j\rangle\langle j|$ for time t and the second backward propagation is under an electronic coherence $|j\rangle\langle k|$ for time $t' = t - \tau$.

Now we derive the quantum-mechanical NE-FGR expression for a normal mode subject to multi-state shifted harmonic potentials (extension to multiple nuclear dimensions will be performed in the following section), where the nuclear Hamiltonian of the i-th normal mode on the j-th electronic state is given by

$$\hat{H}_j = \frac{\hat{p}_i^2}{2} + \frac{1}{2}\omega_i^2(\hat{x}_i - s_j)^2, \quad (j = 1,\ldots,F). \tag{14}$$

We assume that the initial nuclear density $\hat{\rho}(0)$ is the equilibrium distribution of the unshifted ground-state harmonic potential, $\hat{H}_0$,

$$\hat{\rho}(0) = \frac{1}{Z_0} e^{-\beta \hat{H}_0}, \tag{15}$$

$$\hat{H}_0 = \frac{\hat{p}_i^2}{2} + \frac{1}{2}\omega_i^2 \hat{x}_i^2, \tag{16}$$

where partition function $Z_0 = \mathrm{Tr}_N[e^{-\beta \hat{H}_0}]$. Note this choice is still general since the equilibrium positions of all other states, $\{s_j | j = 1,\ldots,F\}$, can be shifted such that the initial sampling is around the origin. The real-time propagator and the imaginary-time density matrix element for $\hat{H}_j$ can be derived using the path integral formalism and they can be converted via Wick's rotation $t = -i\beta\hbar$,

which are given by[66,67]

$$
\begin{aligned}
&U(x_b,t;x_a,0) = \langle x_b|e^{-i\hat{H}_j t/\hbar}|x_a\rangle \\
&= \sqrt{\frac{\omega_i}{2\pi i\hbar\sin(\omega_i t)}}\exp\left\{\frac{i\omega_i}{2\hbar\sin(\omega_i t)}\Big[\big((x_a-s_j)^2\right. \\
&\left.+(x_b-s_j)^2\big)\cos(\omega_i t)-2(x_a-s_j)(x_b-s_j)\Big]\right\}, \qquad (17)\\
&\rho(x_b,x_a;\beta) = \langle x_b|e^{-\beta\hat{H}_j}|x_a\rangle \\
&= \sqrt{\frac{\omega_i}{2\pi\hbar\sinh(\beta\hbar\omega_i)}}\exp\left\{-\frac{\omega_i}{2\hbar\sinh(\beta\hbar\omega_i)}\Big[\big((x_a-s_j)^2\right. \\
&\left.+(x_b-s_j)^2\big)\cosh(\beta\hbar\omega_i)-2(x_a-s_j)(x_b-s_j)\Big]\right\}. \qquad (18)
\end{aligned}
$$

Expressed in the real-time path-integral formulation, the quantum TCF $C_{jk,kj}(t,\tau)$ becomes

$$
\begin{aligned}
C_{jk,kj}(t,\tau) =& \frac{|\Gamma_{jk}|^2}{Z_0}\int \mathrm{d}x_0\cdots\mathrm{d}x_4\langle x_0|e^{-\beta\hat{H}_0}|x_1\rangle\langle x_1|e^{i\hat{H}_j t/\hbar}|x_2\rangle \\
&\times\langle x_2|e^{-i\hat{H}_k t/\hbar}|x_3\rangle\langle x_3|e^{i\hat{H}_k\tau/\hbar}|x_4\rangle\langle x_4|e^{-i\hat{H}_j\tau/\hbar}|x_0\rangle, \qquad (19)
\end{aligned}
$$

which can be evaluated by inserting Eqs. 17 and 18 and integrating over all positions. The resulting expression for the generalized TCF $C_{jk,kj}(t,\tau)$ is given below

$$
\begin{aligned}
&C^{\mathrm{exact}}_{jk,kj}(t,\tau) = |\Gamma_{jk}|^2\exp\left\{\frac{\omega_i d_{jk}^2}{2\hbar}\coth\left(\frac{\beta\hbar\omega_i}{2}\right)\right. \\
&\times[\cos(\omega_i t-\omega_i\tau)-1]+i\cdot\frac{\omega_i}{2\hbar}\Big[-d_{jk}^2\sin(\omega_i t-\omega_i\tau) \\
&\left.+2d_{jk}s_j[\sin(\omega_i t)-\sin(\omega_i\tau)]\Big]\right\}, \qquad (20)
\end{aligned}
$$

where $d_{jk}=s_j-s_k$. Note that the above expression of $C_{DA,AD}(t,\tau)$ reduces to $C(t,t-\tau)$ in Eq. 48 of Ref. 46 with $jk=DA$, $s_j=S$, $s_k=R^{eq}+S$ for each normal mode.

2.2 Semiclassical approximations for NE-FGR

In this section, we derive a series of semiclassical approximations for the generalized TCF $C_{jk,kj}(t,\tau)$ following Ref. 46. The LSC approximation for $C_{jk,kj}(t,\tau)$ is given by

$$C_{jk,kj}^{\text{W-AV}}(t,\tau) = |\Gamma_{jk}|^2 \int \mathrm{d}\mathbf{R}_0 \mathrm{d}\mathbf{P}_0 \, \rho_{0,W}(\mathbf{R}_0,\mathbf{P}_0) \times \exp\left[-\frac{i}{\hbar}\int_t^\tau U_{jk}(\mathbf{R}(u)_{jk})\mathrm{d}u\right], \tag{21}$$

where the initial nuclear sampling is performed with Wigner transformed $\hat{\rho}(0)$, i.e.,

$$\rho_{0,W}(\mathbf{R}_0,\mathbf{P}_0) = \int \mathrm{d}\mathbf{Z}\, e^{-i\mathbf{Z}\cdot\mathbf{P}_0/\hbar} \left\langle \mathbf{R}_0 + \frac{\mathbf{Z}}{2}\middle|\, \hat{\rho}(0) \,\middle| \mathbf{R}_0 - \frac{\mathbf{Z}}{2}\right\rangle. \tag{22}$$

Starting from the sampled initial nuclear conditions $(\mathbf{R}_0,\mathbf{P}_0)$, the system is propagated forwardly during time $0 \to t$ on the j-th PES arriving at $(\mathbf{R}(t)_j, \mathbf{P}(t)_j)$ as in classical MD simulation, and then propagate backwardly during time $t \to \tau$ on the average PES between the j-th and the k-th states, $\overline{V}_{jk}(\mathbf{R}) = \frac{1}{2}\left[V_j(\mathbf{R}) + V_k(\mathbf{R})\right]$ arriving at $(\mathbf{R}(\tau)_{jk}, \mathbf{P}(\tau)_{jk})$. During the second propagation, a phase factor is formed due to the quantum coherence $|j\rangle\langle k|$, which depends on the energy gap between the two PESs defined as

$$U_{jk}(\mathbf{R}) = V_j(\mathbf{R}) - V_k(\mathbf{R}). \tag{23}$$

For the fact that the Wigner initial sampling and then the coherence dynamics on the average PES are employed, we label the LSC approximation as "W-AV".

Replacing the Wigner initial sampling $\rho_{0,W}(\mathbf{R}_0,\mathbf{P}_0)$ in Eq. 21 with the corresponding classical distribution $\rho_{0,Cl}(\mathbf{R}_0,\mathbf{P}_0)$ and still using the same average PES $\overline{V}_{jk}(\mathbf{R})$ for backward propagation

during the quantum coherence period for time $t \to \tau$, we arrive at the "C-AV" approximation:

$$C_{jk,kj}^{\text{C-AV}}(t,\tau) = |\Gamma_{jk}|^2 \int \mathrm{d}\mathbf{R}_0 \mathrm{d}\mathbf{P}_0 \, \rho_{0,Cl}(\mathbf{R}_0,\mathbf{P}_0) \times \exp\left[-\frac{i}{\hbar}\int_t^\tau U_{jk}(\mathbf{R}(u)_{jk})\mathrm{d}u\right]. \tag{24}$$

If we perform the nuclear dynamics during the quantum coherence period on the ground-state PES, or $V_0(\mathbf{R})$, starting from $\mathbf{R}(t)_j$ the nuclear positions arrive at $\mathbf{R}(\tau)_0$. In this case, both W-AV and C-AV approximations become the "W-G" and "C-G" approximations, respectively:

$$C_{jk,kj}^{\text{W-G}}(t,\tau) = |\Gamma_{jk}|^2 \int \mathrm{d}\mathbf{R}_0 \mathrm{d}\mathbf{P}_0 \, \rho_{0,W}(\mathbf{R}_0,\mathbf{P}_0) \times \exp\left[-\frac{i}{\hbar}\int_t^\tau U_{jk}(\mathbf{R}(u)_0)\mathrm{d}u\right], \tag{25}$$

$$C_{jk,kj}^{\text{C-G}}(t,\tau) = |\Gamma_{jk}|^2 \int \mathrm{d}\mathbf{R}_0 \mathrm{d}\mathbf{P}_0 \, \rho_{0,Cl}(\mathbf{R}_0,\mathbf{P}_0) \times \exp\left[-\frac{i}{\hbar}\int_t^\tau U_{jk}(\mathbf{R}(u)_0)\mathrm{d}u\right]. \tag{26}$$

If the relaxation of the nuclear DOF is much slower than the electronic dephasing time, then we reach the inhomogeneous limit, where the nuclear positions will be assumed stationary or after the initial population dynamics on the j-th PES. In this way, we have "W-0" and "C-0" approximations with Wigner and classical initial sampling choices, respectively:

$$C_{jk,kj}^{\text{W-0}}(t,\tau) = |\Gamma_{jk}|^2 \int \mathrm{d}\mathbf{R}_0 \mathrm{d}\mathbf{P}_0 \, \rho_{0,W}(\mathbf{R}_0,\mathbf{P}_0) \times \exp\left[\frac{i}{\hbar}U_{jk}(\mathbf{R}(t)_j)(t-\tau)\right], \tag{27}$$

$$C_{jk,kj}^{\text{C-0}}(t,\tau) = |\Gamma_{jk}|^2 \int \mathrm{d}\mathbf{R}_0 \mathrm{d}\mathbf{P}_0 \, \rho_{0,Cl}(\mathbf{R}_0,\mathbf{P}_0) \times \exp\left[\frac{i}{\hbar}U_{jk}(\mathbf{R}(t)_j)(t-\tau)\right]. \tag{28}$$

3 Multi-State Harmonic (MSH) Model Hamiltonian

The general F-state MSH model Hamiltonian has the same overall diabatic form with nonvanishing off-diagonal electronic couplings as in Eq. 9, but in the MSH model the nuclear Hamiltonians of the F electronic states are given by

$$
\begin{aligned}
\hat{H}_1 &= \sum_{a=1}^{F-1}\sum_{j=1}^{N}\frac{\hat{P}_{a,j}^2}{2} + \sum_{j=1}^{N}\frac{1}{2}\omega_j^2\left[\hat{R}_{1,j}^2+\hat{R}_{2,j}^2+\cdots+\hat{R}_{F-1,j}^2\right]+\varepsilon_1,\\
\hat{H}_2 &= \sum_{a=1}^{F-1}\sum_{j=1}^{N}\frac{\hat{P}_{a,j}^2}{2} + \sum_{j=1}^{N}\frac{1}{2}\omega_j^2\left[\left(\hat{R}_{1,j}-S_j^{(12)}\right)^2+\hat{R}_{2,j}^2+\cdots+\hat{R}_{F-1,j}^2\right]+\varepsilon_2,\\
\hat{H}_3 &= \sum_{a=1}^{F-1}\sum_{j=1}^{N}\frac{\hat{P}_{a,j}^2}{2} + \sum_{j=1}^{N}\frac{1}{2}\omega_j^2\left[\left(\hat{R}_{1,j}-S_j^{(13)}\right)^2+\left(\hat{R}_{2,j}-S_j^{(23)}\right)^2+\cdots+\hat{R}_{F-1,j}^2\right]+\varepsilon_3,\\
&\cdots\\
\hat{H}_F &= \sum_{a=1}^{F-1}\sum_{j=1}^{N}\frac{\hat{P}_{a,j}^2}{2} + \sum_{j=1}^{N}\frac{1}{2}\omega_j^2\left[\left(\hat{R}_{1,j}-S_j^{(1F)}\right)^2+\left(\hat{R}_{2,j}-S_j^{(2F)}\right)^2+\cdots+\left(\hat{R}_{F-1,j}-S_j^{(F-1,F)}\right)^2\right]+\varepsilon_F.
\end{aligned}
\tag{29}
$$

Here, $\{\omega_j | j=1,\ldots,N\}$ are the N physical normal mode frequencies of the globally shared bath; the index $a=1,\ldots,F-1$ labels the $F-1$ extended sets of the physical normal modes resulting in the total nuclear DOF $N_n=(F-1)\times N$; $\{S_j^{(XY)}|1\le X<Y\le F\}$ are the equilibrium (horizontal) shift components for the PES of state Y along the j-th mode; $\{\varepsilon_X|X=1,\ldots,F\}$ are the energy minima (vertical shifts) of the PESs of the different electronic states; $\{\hat{V}_{XY}|X,Y\in(1,\ldots,F),X\neq Y\}$ are the interstate electronic couplings and $\hat{V}_{XY}=\hat{V}_{YX}=\Gamma_{XY}$ is constant under the Condon approximation.

In Ref. 51, we introduced the general way for constructing the MSH model Hamiltonian from multi-state all-atom MD simulations and quantum chemistry calculations. Basically, one needs excited-state electronic structure calculations to determine the excitation energy and the charge distribution for each electronic state, and MD simulations to determine the energy-gap TCF

between all possible pairs of states,

$$C_{UU}^{(XY)}(t) = \langle U_{XY}(t)U_{XY}(0)\rangle - \langle U_{XY}\rangle^2, \tag{30}$$

where the energy gap $U_{XY} = V_X - V_Y$, and V_X and V_Y denote PESs of distinct state X and state Y. More precisely, to construct the F-state harmonic model, the following $F(F-1)/2$ energy-gap TCFs are required: $\{C_{UU}^{(XY)}(t)|X < Y,$ and $X,Y \in 1,\ldots,F\}$. From each TCF, the corresponding reorganization energy between X,Y states is given by

$$E_r^{(XY)} = \frac{C_{UU}^{(XY)}(0)}{2k_BT}. \tag{31}$$

The electronic couplings $\{\Gamma_{XY}\}$ can be obtained from the fragment charge difference (FCD) method.[68] The energy minima $\{\varepsilon_X\}$ are determined from their difference, or the reaction free energies $\Delta E^{(XY)}$, which can be estimated with the reorganization energy and the energy-gap average from equilibrium MD simulations on the PES of the initial electronic state

$$\varepsilon_Y - \varepsilon_X = \Delta E^{(XY)} = -E_r^{(XY)} - \langle U_{XY}\rangle. \tag{32}$$

Using the classical MD for TCF is usually valid for condensed-phase systems since most of the contributing modes are intermolecular vibrations with low frequencies in the THz region.

The $F(F-1)/2$ sets of the equilibrium shift components, or $\{S_j^{(12)}, S_j^{(13)}, S_j^{(23)}, \ldots, S_j^{(F-1,F)}\}$ are designed such that the $F(F-1)/2$ reorganization energy restrictions are satisfied simultaneously. In particular, the $\{S_j^{(XY)}\}$ are chosen such that the distance between the minima of all pairs of PESs scales linearly with the square root of the corresponding reorganization energy:

$$R_j^{(XY)} = \sqrt{\frac{2E_r^{(XY)}}{N}}\frac{1}{\omega_j} = a_j\sqrt{E_r^{(XY)}}, \ \ (j = 1,\ldots,N), \tag{33}$$

where $a_j = \sqrt{2/N}/\omega_j$. The general formulas for the equilibrium shift components $\{S_j^{(XY)}\}$ are

detailed in Ref. 51. In the $F = 4$ state case, which we will use in this work, $\{S_j^{(XY)}\}$ parameters are given by

$$
\begin{aligned}
S_j^{(12)} &= a_j \sqrt{E_r^{(12)}}, \\
S_j^{(13)} &= a_j \sqrt{E_r^{(13)}} \cos\theta_{23}, \\
S_j^{(23)} &= a_j \sqrt{E_r^{(13)}} \sin\theta_{23}, \\
S_j^{(14)} &= a_j \sqrt{E_r^{(14)}} \cos\theta_{24}, \\
S_j^{(24)} &= a_j \sqrt{E_r^{(14)}} \sin\theta_{24} \cos\theta'_{34}, \\
S_j^{(34)} &= a_j \sqrt{E_r^{(14)}} \sin\theta_{24} \sin\theta'_{34},
\end{aligned}
\tag{34}
$$

where

$$
\cos\theta_{jk} = \frac{E_r^{(1j)} + E_r^{(1k)} - E_r^{(jk)}}{2\sqrt{E_r^{(1j)} E_r^{(1k)}}}, \tag{35}
$$

$$
\cos\theta'_{3k} = \frac{\cos\theta_{3k} - \cos\theta_{23}\cos\theta_{2k}}{\sin\theta_{23}\sin\theta_{2k}}, \ (k \geq 4). \tag{36}
$$

We briefly comment on the MSH model. First, the MSH model in Eq. 29 is not a conventional harmonic model, but a special one with the parameters that are designed for consistently incorporating the multi-state characteristics of the interstate correlations, in terms of reorganization energies between all possible *pairs of states*. Conventional harmonic models like the Frenkel exciton model only account for the correlations between the excited states and the ground state, but not between any pair of excited states.[53] Second, the interstate correlations are achieved by extending the spatial dimension for *each normal mode* to $F-1$ dimensions, which are required to fully represent the reorganization energies corresponding to the $F(F-1)/2$ pairs of states in an F-state system. The resulting $(F-1)\times N$ total nuclear DOF are still representing the N physical normal modes but in an extended space.[51] Third, the MSH model parameters are constructed from mapping all-atom simulations, rather than some assumed analytical form for spectral density. The MSH model of the triad system has been demonstrated to agree with the all-atom semiclassical nonadiabatic dynamics described by about explicit 88,000 atoms, suggesting that MSH model is

useful in estimating the timescales of electronic transition and the significance of nuclear quantum effects cost-effectively.[52] However, the MSH model has limitations. For instance, it cannot provide atomistic information and the nuclear normal mode frequencies are obtained by discretizing a spectral density into finite N modes, thereby the Duschinsky rotation effects are neglected and only the irreversible dissipative dynamics in timescales shorter than the Poincaré recurrence time is physical.

To simplify the notation for NE-FGR expressions for the MSH model, we recast the MSH model Hamiltonian in Eq. 29 as below. First, we extend the equilibrium shift parameters by setting $\{S_j^{(XY)}\} \equiv 0$ when $X \geq Y$. Second, we rewrite the nuclear Hamiltonian of the X-th electronic state, i.e., $\hat{H}_X$ $(X = 1,\ldots,F)$ using the composite index i for nuclear DOF as in the mapping relation $(a,j) \to i$, where $i = 1,\ldots,N_n$ and $N_n = (F-1)N$ such that $(\hat{P}_{a,j}, \hat{R}_{a,j}) \to (\hat{R}_i, \hat{P}_i)$ and $S_j^{(aX)} \to S_i^{(X)}$:

$$\hat{H}_X = \sum_{a=1}^{F-1} \sum_{j=1}^{N} \left[\frac{\hat{P}_{a,j}^2}{2} + \frac{1}{2}\omega_j^2 \left(\hat{R}_{a,j} - S_j^{(aX)} \right)^2 \right] + \varepsilon_X \tag{37}$$

$$\equiv \sum_{i=1}^{N_n} \left[\frac{\hat{P}_i^2}{2} + \frac{1}{2}\omega_i^2 \left(\hat{R}_i - S_i^{(X)} \right)^2 \right] + \varepsilon_X. \tag{38}$$

Third, we denote $D_i^{(XY)} \equiv S_i^{(X)} - S_i^{(Y)}$ and $\hbar\omega_{XY} = \varepsilon_X - \varepsilon_Y$ for $X, Y = 1,\ldots,F$ and $X \neq Y$. Using the similar technique described in Ref. 46, we have the closed-form expressions of TCF on the

above-mentioned generalized NE-FGR approximation levels for the MSH model:

$$C_{jk,kj}^{\text{exact/W-AV}}(t,\tau) = |\Gamma_{jk}|^2 \exp\left\{ i\omega_{jk}(t-\tau) + \sum_{i=1}^{N_n} \frac{\omega_i (D_i^{(jk)})^2}{2\hbar} \coth\left(\frac{\beta\hbar\omega_i}{2}\right) [\cos(\omega_i t - \omega_i \tau) - 1] \right.$$
$$\left. + i \cdot \sum_{i=1}^{N_n} \frac{\omega_i}{2\hbar} \left[-(D_i^{(jk)})^2 \sin(\omega_i t - \omega_i \tau) + 2 D_i^{(jk)} S_i^{(j)} [\sin(\omega_i t) - \sin(\omega_i \tau)] \right] \right\}, \tag{39}$$

$$C_{jk,kj}^{\text{C-AV}}(t,\tau) = |\Gamma_{jk}|^2 \exp\left\{ i\omega_{jk}(t-\tau) + \sum_{i=1}^{N_n} \frac{(D_i^{(jk)})^2}{\beta\hbar^2} [\cos(\omega_i t - \omega_i \tau) - 1] \right.$$
$$\left. + i \cdot \sum_{i=1}^{N_n} \frac{\omega_i}{2\hbar} \left[-(D_i^{(jk)})^2 \sin(\omega_i t - \omega_i \tau) + 2 D_i^{(jk)} S_i^{(j)} [\sin(\omega_i t) - \sin(\omega_i \tau)] \right] \right\}, \tag{40}$$

$$C_{jk,kj}^{\text{W-G}}(t,\tau) = |\Gamma_{jk}|^2 \exp\left\{ i\omega_{jk}(t-\tau) + \sum_{i=1}^{N_n} \frac{\omega_i (D_i^{(jk)})^2}{2\hbar} \coth\left(\frac{\beta\hbar\omega_i}{2}\right) [\cos(\omega_i t - \omega_i \tau) - 1] \right.$$
$$\left. + i \cdot \sum_{i=1}^{N_n} \frac{\omega_i}{2\hbar} \left[\left((S_i^{(j)})^2 - (S_i^{(k)})^2 \right) (\omega_i t - \omega_i \tau) + 2 D_i^{(jk)} S_i^{(j)} [\sin(\omega_i t) - \sin(\omega_i \tau) - \sin(\omega_i t - \omega_i \tau)] \right] \right\}, \tag{41}$$

$$C_{jk,kj}^{\text{C-G}}(t,\tau) = |\Gamma_{jk}|^2 \exp\left\{ i\omega_{jk}(t-\tau) + \sum_{i=1}^{N_n} \frac{(D_i^{(jk)})^2}{\beta\hbar^2} [\cos(\omega_i t - \omega_i \tau) - 1] \right.$$
$$\left. + i \cdot \sum_{i=1}^{N_n} \frac{\omega_i}{2\hbar} \left[\left((S_i^{(j)})^2 - (S_i^{(k)})^2 \right) (\omega_i t - \omega_i \tau) + 2 D_i^{(jk)} S_i^{(j)} [\sin(\omega_i t) - \sin(\omega_i \tau) - \sin(\omega_i t - \omega_i \tau)] \right] \right\}, \tag{42}$$

$$C_{jk,kj}^{\text{W-0}}(t,\tau) = |\Gamma_{jk}|^2 \exp\left\{ i\omega_{jk}(t-\tau) + \sum_{i=1}^{N_n} \frac{\omega_i (D_i^{(jk)})^2}{2\hbar} \coth\left(\frac{\beta\hbar\omega_i}{2}\right) \left[-\frac{1}{2} (\omega_i t - \omega_i \tau)^2 \right] \right.$$
$$\left. + i \cdot \sum_{i=1}^{N_n} \frac{\omega_i}{2\hbar} \left[-(D_i^{(jk)})^2 (\omega_i t - \omega_i \tau) + 2 D_i^{(jk)} S_i^{(j)} (\omega_i t - \omega_i \tau) \cos(\omega_i t) \right] \right\}, \tag{43}$$

$$C_{jk,kj}^{\text{C-0}}(t,\tau) = |\Gamma_{jk}|^2 \exp\left\{ i\omega_{jk}(t-\tau) + \sum_{i=1}^{N_n} \frac{(D_i^{(jk)})^2}{\beta\hbar^2} \left[-\frac{1}{2} (\omega_i t - \omega_i \tau)^2 \right] \right.$$
$$\left. + i \cdot \sum_{i=1}^{N_n} \frac{\omega_i}{2\hbar} \left[-(D_i^{(jk)})^2 (\omega_i t - \omega_i \tau) + 2 D_i^{(jk)} S_i^{(j)} (\omega_i t - \omega_i \tau) \cos(\omega_i t) \right] \right\}. \tag{44}$$

It is important to note that for the MSH model, the LSC expression of NE-FGR is identical to the exact quantum-mechanical NE-FGR formula, thus we will plot the exact NE-FGR and the LSC (W-AV) results together in the result section. Note that perturbative NE-FGR is expected to be valid when the electronic couplings are weak in MSH model.

The MSH models of two conformations of the CPC_{60} triad with four electronic states,

$\{\pi\pi^*, \mathrm{CT1}, \mathrm{CT2}, \mathrm{G}\}$ were developed in Ref. 52, and the energy minima and interstate electronic couplings parameters are summarized in Table 1. The triad conformations are selected from the CT landscape landmark structure database,[64] and here Conf. #2 and Conf. #3 as shown in Fig. 2 are adopted from Refs. 51 and 52, which show very different photoinduced CT dynamics, for example, Conf. #3 has CT2 state populated in the first picoseconds but Conf. #2 does not. Since the ground state is only for initial nuclear sampling and it does not have electronic couplings with the three excited states in the model, the energy minimum parameter ε_G does not affect the dynamics thus can be chosen arbitrarily. The number of physical normal modes $N = 200$ and for the four-state MSH model, the total nuclear DOF is $N_n = (F-1)N = 600$. Two temperatures for the liquid solution phase were investigated: room temperature at $T = 300$ K and a low temperature at $T = 200$ K, which is still above the freezing point of THF (164 K). The initial state for the nuclear DOF was chosen as the equilibrated ground state on the PES $V_G(\mathbf{R})$, where the semiclassical Wigner distribution was employed in W-AV, W-G, and W-0 methods and the classical distribution was employed in C-AV, C-G, and C-0 methods. The initial electronic state is a population of $|\pi\pi^*\rangle\langle\pi\pi^*|$, which mimics the result of vertical excitation from the ground state to the $\pi\pi^*$ state. The nuclear time step is $\Delta t = 0.1$ fs and the total length of propagation is 2 ps. The memory time τ_m, beyond which the TCF is assumed to vanish, is tested and chosen to be 0.04 ps and 0.25 ps for conformations #2 and #3, respectively (see supporting information). The frequencies and equilibrium shifts of the MSH models are provided in supporting information.

4 Results and Discussion

In this section, we present the results for the photoinduced CT dynamics in the MSH models of CPC_{60} triad calculated by the generalized NE-FGR approach. Although different levels of approximation of NE-FGR may have a similar computational cost for the MSH models, it is important to note that the more classical NE-FGR approaches are much cheaper than the more quantum NE-FGR approaches in realistic all-atom systems, like solar energy conversion materials.

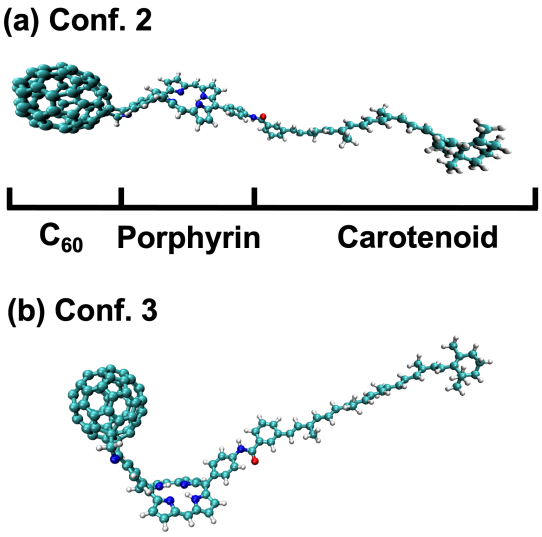

Figure 2: Conformations of CPC_{60} triad studied here, (a) conformation #2 and (b) conformation #3.

Table 1: Energy minima ε_X for the excited states and the interstate electronic couplings Γ_{XY} between different pairs of states in two conformations (#2 and #3) of the triad (in eV). Here, electronic states $X = 1,2,3,4$ corresponding to $\pi\pi^*$, CT1, CT2, and ground states, respectively. The electronic couplings between any excited states $(j < 4)$ and the ground state are assumed to be zero.

state	Conf. #2	Conf. #3
$\varepsilon(\pi\pi^*)$	0	0
$\varepsilon(\mathrm{CT1})$	-0.268	-0.828
$\varepsilon(\mathrm{CT2})$	-0.779	-0.640
Γ_{12}	8.8×10^{-2}	-1.5×10^{-2}
Γ_{13}	1.1×10^{-4}	7.2×10^{-3}
Γ_{23}	1.2×10^{-4}	-2.9×10^{-2}
Γ_{j4}	0	0

Thus, it is essential to test the accuracy of different approximation levels of NE-FGR in MSH model, where the fully quantum-mechanical expression is available. This study serves as a demonstration of how to benchmark for NE-FGR semiclassical approaches and can be used in other systems since the applicability of approximations varies from system to system.

The photoinduced process starts out with a vertical excitation from an equilibrated ground state triad dissolved in THF solvent and time zero starts from 100% electronic population on the $\pi\pi^*$ state. Following the instantaneous photoexcitation, the nuclear DOF start to relax and the nonadiabatic transition pathways between any pair of excited states are possible, i.e., $\pi\pi^*$, CT1, and CT2 states. The two conformations of the triad investigated here are Conf. #2 and Conf. #3, and their photoinduced CT dynamics at the high temperature of 300 K and the low temperature of 200 K are shown in Figs. 3–6. A general observation is that the dynamics of the selected triad conformations are quite different. In Conf. #2, the main population transfer is through the pathway $\pi\pi^* \rightarrow$ CT1 in the first 0.5 ps after photoexcitation, which means the local excitation energy is converted to the charge transfer with hole localized on porphyrin and electron localized on C_{60}. On the contrary, Conf. #3 gives a different photoinduced CT picture, where the CT2 state also gets populated resulting carotenoid-localized hole ($\pi\pi^* \rightarrow$ CT2 pathway) besides porphyrin-localized hole ($\pi\pi^* \rightarrow$ CT1 pathway). This can be explained by a shorter distance between C_{60} and carotenoid in Conf. #3 than in Conf. #2 helps stabilize the carotenoid-to-C_{60} CT2 state in Conf. 3. More detailed discussions on the atomistic details of photoinduced CT in the triad in an explicit solvent can be found in the previous work.[48,52]

In particular, the population dynamics at different NE-FGR levels for the triad Conf. #2 at 300 K are reported in Fig. 3. It is evident that the population is transferred from the $\pi\pi^*$ state to the CT1 state, while the CT2 state stays unpopulated for the first 2 ps (not shown) after the photoexcitation. This can be understood by comparing the electronic couplings for different pairs of states of triad Conf. #2 in Table 1, where the coupling between $\pi\pi^*$ and CT1 is $\Gamma_{\pi\pi^*,\mathrm{CT1}} = 8.8 \times 10^{-2}$ eV, two orders of magnitude larger than $\Gamma_{\pi\pi^*,\mathrm{CT2}} = 1.1 \times 10^{-4}$ eV and $\Gamma_{\mathrm{CT1,CT2}} = 1.2 \times 10^{-4}$ eV. The $\pi\pi^*$ population suddenly drops at an ultrafast time and then shows a non-monotonic trend in the first

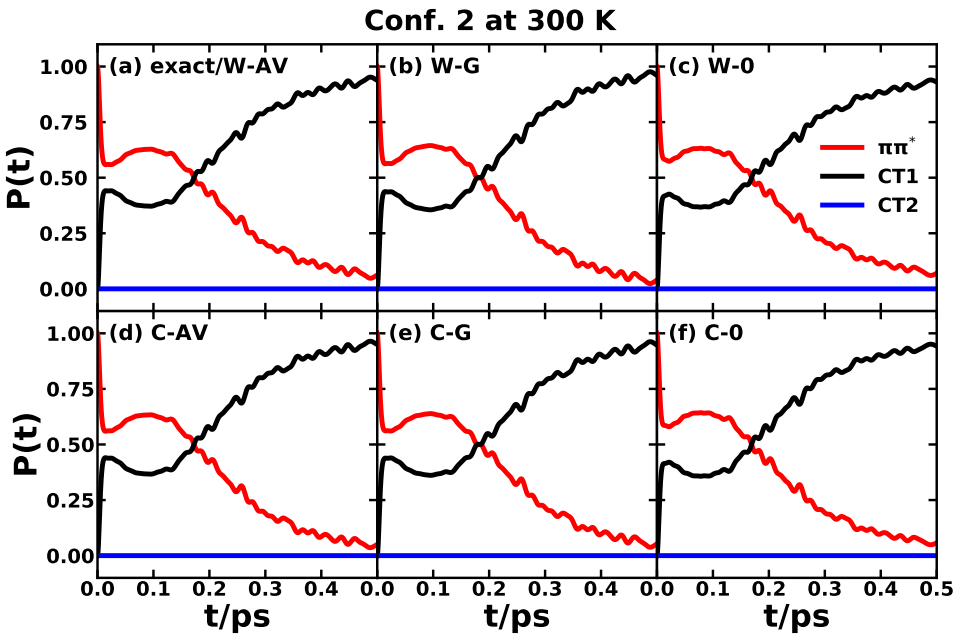

Figure 3: Photoinduced CT population dynamics for the MSH model of the CPC_{60} triad conformation #2 obtained with different levels of NE-FGR at 300 K. The initial electronic state is $\pi\pi^*$ and the initial nuclear state is in thermal equilibrium with the ground state potential energy surface.

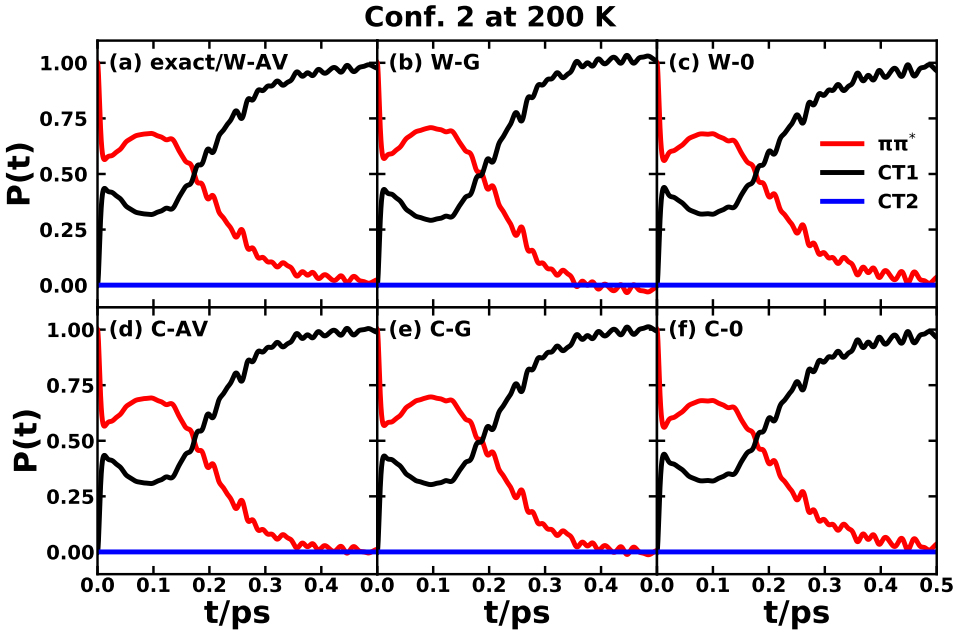

Figure 4: Photoinduced CT population dynamics for the MSH model of the CPC_{60} triad conformation #2 obtained with different levels of NE-FGR at 200 K. The initial electronic state is $\pi\pi^*$ and the initial nuclear state is in thermal equilibrium with the ground state potential energy surface.

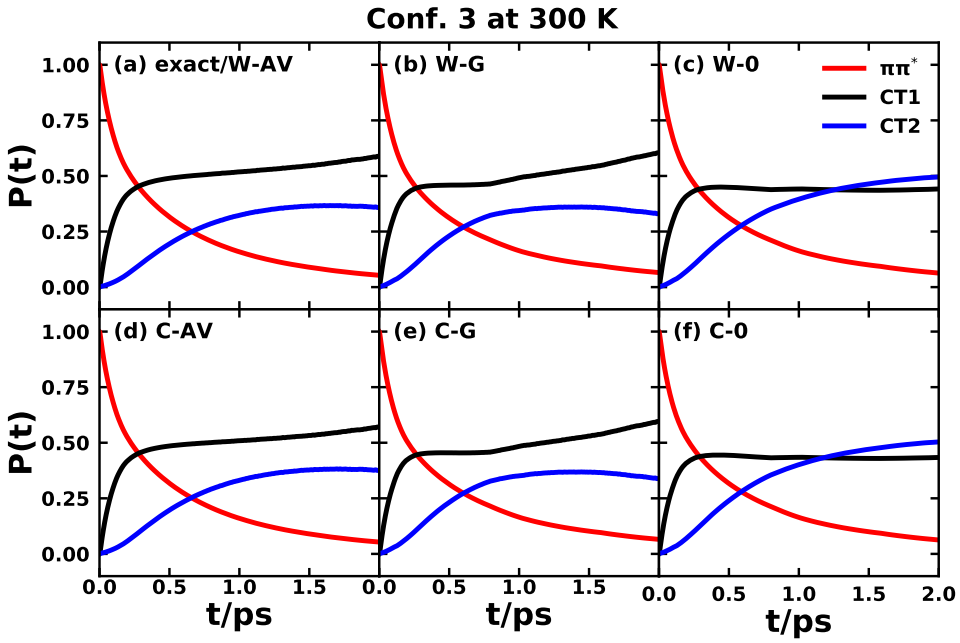

Figure 5: Photoinduced CT population dynamics for the MSH model of the CPC_{60} triad conformation #3 obtained with different levels of NE-FGR at 300 K. The initial electronic state is $\pi\pi^*$ and the initial nuclear state is in thermal equilibrium with the ground state potential energy surface.

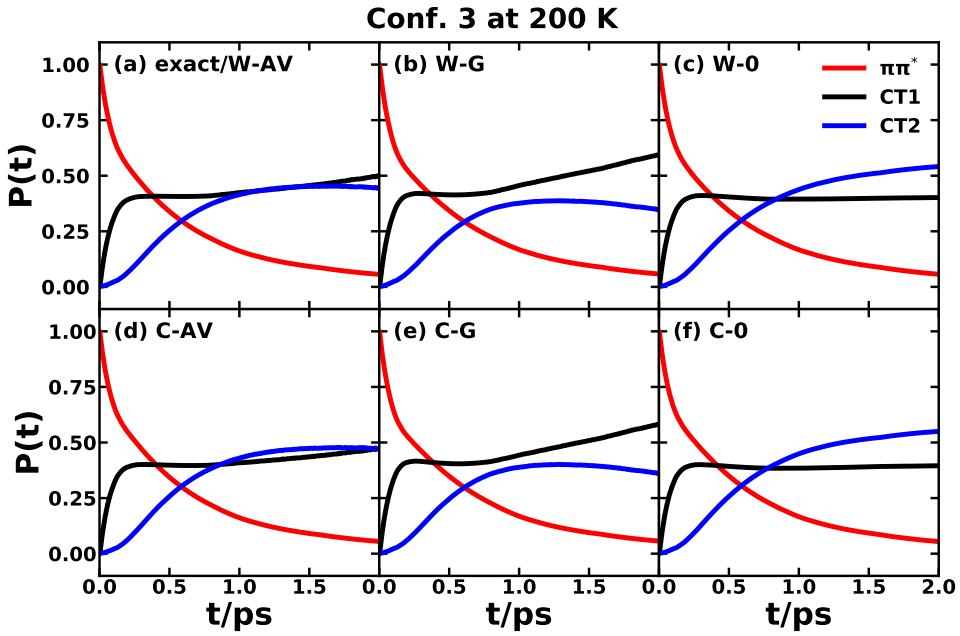

Figure 6: Photoinduced CT population dynamics for the MSH model of the CPC_{60} triad conformation #3 obtained with different levels of NE-FGR at 200 K. The initial electronic state is $\pi\pi^*$ and the initial nuclear state is in thermal equilibrium with the ground state potential energy surface.

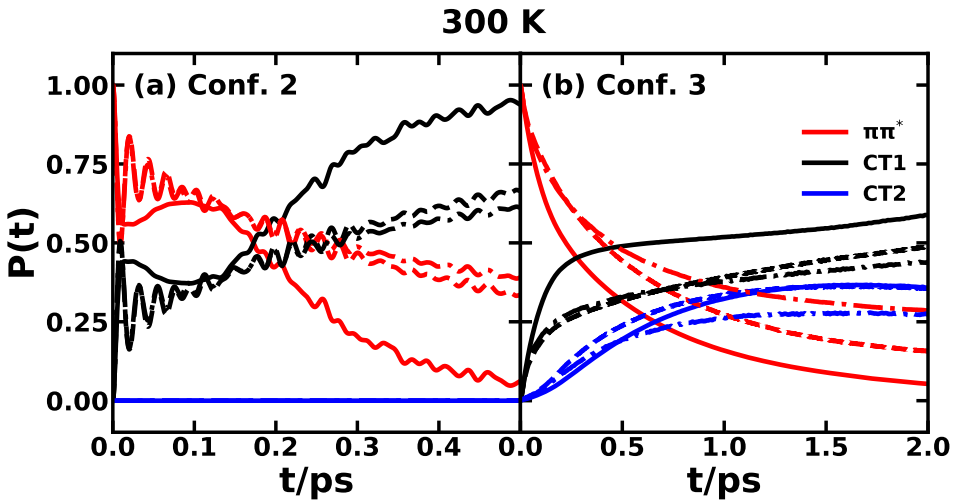

Figure 7: Comparison of population dynamics between the exact NE-FGR and nonadiabatic dynamics using the symmetrical quasiclassical with triangle window (SQC) and the resolution-of-identity linearized semiclassical (RI-LSC1)[52] for the MSH models of the triad conformations #2 and #3 at 300 K.

0.2 ps, where the population decay rate of $\pi\pi^*$ and CT1 is reversed briefly before getting back to normal population transfer direction, that is $\pi\pi^* \rightarrow$ CT1. Different NE-FGR approximations seem able to capture the exact NE-FGR dynamics well, even on the C-0 level, where we assume no semiclassical Wigner nuclear sampling and no dynamics in the quantum coherence period. Fig. 4 displays the NE-FGR results for Conf. #2 at 200 K. Comparing 200 K against 300 K results, we observe a faster population decay timescale of about 0.3 ps at 200 K than about 0.5 ps at 300 K. Besides, at the low temperature, we observe that W-G and C-G approximations give a slightly negative population for $\pi\pi^*$ state briefly around 0.5 ps, but then get back to physical positive values at a later time, which can be traced back to the fact that the governing PES is assumed to be that of the ground state during the quantum coherence period. In contrast, W-0 and C-0 do not seem to have this type of issue and both approaches give reasonable population dynamics that agree with the exact NE-FGR or LSC (W-AV) predictions.

What is more interesting is the triad Conf. #3 as shown in Fig. 5 for 300 K, which displays an ultrafast population transfer between all three excited states. This phenomenon is expected since the couplings between all pairs of states are comparable within an order of magnitude (10^{-3} to

10^{-2} eV, see Table 1), so the population transfer rates from the $\pi\pi^*$ state to both of the CT1 and CT2 states are comparable. The initial rise of the population in the CT1 state in the exact NE-FGR at 300 K indicates a larger instantaneous rate coefficient of $k_{\pi\pi^*\to\mathrm{CT1}}(t)$ than $k_{\pi\pi^*\to\mathrm{CT2}}(t)$ in the first 0.5 ps, and then the CT2 state gets populated while the CT1 population gets flattened. Comparing different approximation levels, the Wigner sampling and the classical sampling for the nuclear DOF seem not to make a large difference, since the W-AV and C-AV population dynamics are almost identical. So are the W-G and C-G approaches as well as the W-0 and C-0 approaches. However, comparing the different coherence dynamics such as W-AV, W-G, and W-0, we do see a noticeable difference, especially W-G gives a higher CT1 population and W-0 gives a lower CT1 population at a long time compared with the exact NE-FGR or W-AV result. At the lower temperature of 200 K as shown in Fig. 6, we observe a similar trend but a slower overall population transfer rate as compared with the high-temperature case.

Considering the computational expense of the classical sampling versions C-AV, C-G, and C-0, they provide a great option for complex condensed-phase systems, since the classical sampling is more straightforward in MD simulations than the Wigner sampling, especially when nuclear quantum effects are not significant such as at high temperatures. Among all the approximations, C-0 is attractive and the most straightforward for implementation, since it is based on classical sampling on the ground state or any nuclear initial state, and in the meanwhile, the only dynamics that one has to propagate is the nonequilibrium relaxation on the j-th state's PES during the population $|j\rangle\langle j|$, and no further dynamics is needed for the following coherence period. We believe that the C-0 level of theory can also be generated to the Marcus level, or the instantaneous Marcus theory,[48,49] but this is out of the scope of the current work and will be reported in future work.

Fig. 7 shows the comparison between the NE-FGR and nonadiabatic semiclassical dynamics based on the mapping basis,[69,70] such as the symmetrical quasiclassical (SQC) dynamics[71–76] with triangle window functions[74,76] as well as the resolution-of-identity linearized semiclassical dynamics (RI-LSC1)[77–79] obtained from Ref. 52. For the triad Conf. #2, the NE-FGR $\pi\pi^*$

population curve tracks the lower profile of the semiclassical results, which suggests that an explicit treatment to the quantum coherence-to-population mechanisms might be required to have more realistic ultrafast population oscillations. After the first 0.3 ps, the NE-FGR population decay is overestimated compared with the two nonadiabatic semiclassical dynamics, SQC and RI-LSC1, which behave similarly. Despite the difference between NE-FGR and the nonadiabatic dynamics included here, we cannot take the nonadiabatic semiclassical dynamics as the ground truth, but as a reference. For the triad Conf. #3, the NE-FGR seems to overestimate the population transfer from the initial $\pi\pi^*$ to the CT1 state, while the difference between SQC and RI-LSC1 is also quite noticeable. In both cases, NE-FGR provides a consistent time scale for the population transfer compared with the two nonadiabatic semiclassical dynamics, which is still quite impressive, since the calculation of NE-FGR is much cheaper than simulating the nonadiabatic dynamics directly. We thus believe NE-FGR could be useful for investigating population transfer dynamics in more complex systems in the condensed phase.

5 Concluding Remarks

In this work, we generalized nonequilibrium Fermi's golden rule (NE-FGR) methodology to simulate the electronic population transitions between multiple states in the newly developed multi-state harmonic (MSH) model Hamiltonian for photoinduced CT in an organic photovoltaic triad, CPC_{60} dissolved in THF. The MSH model Hamiltonians were constructed for different triad conformations, which have different excitation energies and interstate electronic couplings. Closed-form expressions were derived for the general MSH model Hamiltonian, and furthermore, a hierarchy of semiclassical approximations to the fully quantum-mechanical NE-FGR was developed as well. The LSC approximation coincides with the exact quantum-mechanical NE-FGR expression in the perturbative limit for the MSH model. With Wigner or classical nuclear sampling options, we have further proposed W-G, W-0, C-AV, C-G, and C-0 approximation levels, which differ from which PES will be used for nuclear propagation during the quantum coherence

period. Our simulations for two different triad conformations (Conf. #2 and Conf. #3) display that the difference between all levels of approximation for NE-FGR is not too large, especially in the high temperature (300 K) case, where the nuclear quantum effect is not significant. However, it does not mean that for any system the different approximation levels would give the same result. In fact, the current work serves as a demonstration of how to benchmark for different semiclassical NE-FGR approaches with the help of the MSH model. The benchmark would provide guidance for realistic all-atom systems, like solar energy conversion materials since the more classical approximation NE-FGR approaches are much computationally cheaper than the more quantum NE-FGR approaches, and one could adopt the cheaper approaches if it does not compromise the predicting power. Also, by comparing with nonadiabatic semiclassical dynamics, we see similar timescales predicted by NE-FGR theories. Considering the computational straightforwardness of NE-FGR, we believe the current formulation for the MSH Hamiltonian could provide physical insights for more complex systems, especially the cheapest C-0 approximation among all levels mentioned above. Other extensions could be made for NE-FGR methodology to study quantum dynamics in multi-state systems, such as extending the current time-convolutionless quantum master equations to the time-convolution ones and incorporating quantum coherences in propagation.[65] With the versatile MSH model Hamiltonians for general multi-state molecular systems in the condensed phase, the photoinduced CT and excitation energy transfer processes in heterogeneous nanoscale materials[80–88] and biological systems[7,11,53,89–91] could be investigated.

Supporting Information

See the Supporting Information (SI) for MSH model parameters and example TCFs in both conformations of CPC_{60} triad.

Acknowledgement

X.S. acknowledges support from the National Natural Science Foundation of China (No. 22273059) and the Hefei National Laboratory for Physical Sciences at the Microscale (No. KF2020008). Computing resources were provided by NYU Shanghai HPC.

Conflict of Interest

The authors have no conflicts to disclose.

References

(1) Wang, D.; Fiebig, O. C.; Harris, D.; Toporik, H.; Ji, Y.; Chuang, C.; Nairat, M.; Tong, A. L.; Ogren, J. I.; Hart, S. M.; Cao, J.; Sturgis, J. N.; Mazor, Y.; Schlau-Cohen, G. S. Elucidating Interprotein Energy Transfer Dynamics within the Antenna Network from Purple Bacteria. *Proc. Natl. Acad. Sci. U.S.A.* **2023**, *120*, e2220477120.

(2) Palacino-González, E.; Jansen, T. L. C. Modeling the Effect of Disorder in the Two-Dimensional Electronic Spectroscopy of Poly-3-hexyltiophene in an Organic Photovoltaic Blend: A Combined Quantum/Classical Approach. *J. Phys. Chem. C* **2023**, *127*, 6793–6801.

(3) Wang, J.; Cui, Y.; Chen, Z.; Zhang, J.; Xiao, Y.; Zhang, T.; Wang, W.; Xu, Y.; Yang, N.; Yao, H.; Hao, X.-T.; Wei, Z.; Hou, J. A Wide Bandgap Acceptor with Large Dielectric Constant and High Electrostatic Potential Values for Efficient Organic Photovoltaic Cells. *J. Am. Chem. Soc.* **2023**, *145*, 13686–13695.

(4) Han, G.; Zhang, Y.; Zheng, W.; Yi, Y. Electron Transport in Organic Photovoltaic Acceptor Materials: Improving the Carrier Mobilities by Intramolecular and Intermolecular Modulations. *J. Phys. Chem. Lett.* **2023**, *14*, 4497–4503.

(5) Wang, T.; Chen, Z.-H.; Qiao, J.-W.; Qin, W.; Liu, J.-Q.; Wang, X.-Z.; Pu, Y.-J.; Yin, H.; Hao, X.-T. Correlating Charge Transfer Dynamics with Interfacial Trap States in High-Efficiency Organic Solar Cells. *ACS Appl. Mater. Interfaces* **2023**, *15*, 12109–12118.

(6) Li, Q.; Wang, R.; Zhang, C. The Dynamics of Delocalized Excitations in Organic Solar Cells with Nonfullerene Acceptors. *J. Phys. Chem. Lett.* **2023**, *14*, 3031–3038.

(7) Roy, P. P.; Kundu, S.; Valdiviezo, J.; Bullard, G.; Fletcher, J. T.; Liu, R.; Yang, S.-J.; Zhang, P.; Beratan, D. N.; Therien, M. J.; Makri, N.; Fleming, G. R. Synthetic Control of Exciton Dynamics in Bioinspired Cofacial Porphyrin Dimers. *J. Am. Chem. Soc.* **2022**, *144*, 6298–6310.

(8) Zhang, G.; Lin, F. R.; Qi, F.; Heumüller, T.; Distler, A.; Egelhaaf, H.-J.; Li, N.; Chow, P. C. Y.; Brabec, C. J.; Jen, A. K.-Y.; Yip, H.-L. Renewed Prospects for Organic Photovoltaics. *Chem. Rev.* **2022**, *122*, 14180–14274.

(9) Vauthey, E. Elucidating the Mechanism of Bimolecular Photoinduced Electron Transfer Reactions. *J. Phys. Chem. B* **2022**, *126*, 778–788.

(10) Giannini, S.; Blumberger, J. Charge Transport in Organic Semiconductors: The Perspective from Nonadiabatic Molecular Dynamics. *Acc. Chem. Res.* **2022**, *55*, 819–830.

(11) Romero, E.; Novoderezhkin, V. I.; van Grondelle, R. Quantum Design of Photosynthesis for Bio-Inspired Solar-Energy Conversion. *Nature* **2017**, *543*, 355–365.

(12) Proppe, A. H.; Li, Y. C.; Aspuru-Guzik, A.; Berlinguette, C. P.; Chang, C. J.; Cogdell, R.; Doyle, A. G.; Flick, J.; Gabor, N. M.; Grondelle, R., et al. Bioinspiration in Light Harvesting and Catalysis. *Nat. Rev. Mater.* **2020**, *5*, 828–846.

(13) Ma, Z.; Lin, Z.; Lawrence, C. M.; Rubtsov, I. V.; Antoniou, P.; Skourtis, S. S.; Zhang, P.; Beratan, D. N. How Can Infra-Red Excitation Both Accelerate and Slow Charge Transfer in the Same Molecule? *Chem. Sci.* **2018**, *9*, 6395–6405.

(14) Wan, X.; Li, C.; Zhang, M.; Chen, Y. Acceptor-Donor-Acceptor Type Molecules for High Performance Organic Photovoltaics – Chemistry and Mechanism. *Chem. Soc. Rev.* **2020**, *49*, 2828–2842.

(15) Chen, Z.; Zhu, H. Photoinduced Charge Transfer and Recombination Dynamics in Star Nonfullerene Organic Solar Cells. *J. Phys. Chem. Lett.* **2022**, *13*, 1123–1130.

(16) Prezhdo, O. V. Modeling Non-adiabatic Dynamics in Nanoscale and Condensed Matter Systems. *Acc. Chem. Res.* **2021**, *54*, 4239–4249.

(17) Nelson, T. R.; White, A. J.; Bjorgaard, J. A.; Sifain, A. E.; Zhang, Y.; Nebgen, B.; Fernandez-Alberti, S.; Mozyrsky, D.; Roitberg, A. E.; Tretiak, S. Non-Adiabatic Excited-State Molecular Dynamics: Theory and Applications for Modeling Photophysics in Extended Molecular Materials. *Chem. Rev.* **2020**, *120*, 2215–2287.

(18) Zhang, T.-S.; Fang, Y.-G.; Song, X.-F.; Fang, W.-H.; Cui, G. Hydrogen-Bonding Interaction Regulates Photoisomerization of a Single-Bond-Rotation Locked Photoactive Yellow Protein Chromophore in Protein. *J. Phys. Chem. Lett.* **2020**, *11*, 2470–2476.

(19) May, V.; Kühn, O. *Charge and Energy Transfer Dynamics in Molecular Systems*; Wiley: Weinheim, 2011.

(20) Nitzan, A. *Chemical Dynamics in Condensed Phases: Relaxation, Transfer and Reactions in Condensed Molecular Systems*; Oxford University Press: New York, 2006.

(21) Lin, S. H.; Chang, C. H.; Liang, K. K.; Chang, R.; Shiu, Y. J.; Zhang, J. M.; Yang, T.-S.; Hayashi, M.; Hsu, F. C. *Advances in Chemical Physics*; John Wiley & Sons, Ltd, 2002; Chapter 1, pp 1–88.

(22) Peng, Q.; Yi, Y.; Shuai, Z.; Shao, J. Excited State Radiationless Decay Process with Duschinsky Rotation Effect: Formalism and Implementation. *J. Chem. Phys.* **2007**, *126*, 114302.

(23) Beyer, A. N.; Richardson, J. O.; Knowles, P. J.; Rommel, J.; Althorpe, S. C. Quantum Tunneling Rates of Gas-Phase Reactions from On-the-Fly Instanton Calculations. *J. Phys. Chem. Lett.* **2016**, *7*, 4374–4379.

(24) Chaudhuri, S.; Hedström, S.; Méndez-Hernández, D. D.; Hendrickson, H. P.; Jung, K. A.; Ho, J.; Batista, V. S. Electron Transfer Assisted by Vibronic Coupling from Multiple Modes. *J. Chem. Theory Comput.* **2017**, *13*, 6000–6009.

(25) Heller, E. R.; Richardson, J. O. Instanton Formulation of Fermi's Golden Rule in the Marcus Inverted Regime. *J. Chem. Phys.* **2020**, *152*, 034106.

(26) Saller, M. A. C.; Lai, Y.; Geva, E. Cavity-Modified Fermi's Golden Rule Rate Constants from Cavity-Free Inputs. *J. Phys. Chem. C* **2023**, *127*, 3154–3164.

(27) Liu, Z.; Xu, W.; Tuckerman, M. E.; Sun, X. Imaginary-Time Open-Chain Path-Integral Approach for Two-State Time Correlation Functions and Applications in Charge Transfer. *J. Chem. Phys.* **2022**, *157*, 114111.

(28) Marcus, R. A. On the Theory of Oxidation–Reduction Reactions Involving Electron Transfer. I. *J. Chem. Phys.* **1956**, *24*, 966–978.

(29) Marcus, R. A. Electrostatic Free Energy and Other Properties of States Having Nonequilibrium Polarization. I. *J. Chem. Phys.* **1956**, *24*, 979–989.

(30) Marcus, R. A. Electron Transfer Reactions in Chemistry. Theory and Experiment. *Rev. Mod. Phys.* **1993**, *65*, 599.

(31) Georgievskii, Y.; Hsu, C. P.; Marcus, R. A. Linear Response in Theory of Electron Transfer Reactions as an Alternative to the Molecular Harmonic Oscillator Model. *J. Chem.Phys.* **1999**, *110*, 5307–5317.

(32) Sun, X.; Geva, E. Equilibrium Fermi's Golden Rule Charge Transfer Rate Constants in the

Condensed Phase: The Linearized Semiclassical Method vs Classical Marcus Theory. *J. Phys. Chem. A* **2016**, *120*, 2976–2990.

(33) Sun, X.; Zhang, P.; Lai, Y.; Williams, K. L.; Cheung, M. S.; Dunietz, B. D.; Geva, E. Computational Study of Charge-Transfer Dynamics in the Carotenoid–Porphyrin–C_{60} Molecular Triad Solvated in Explicit Tetrahydrofuran and Its Spectroscopic Signature. *J. Phys. Chem. C* **2018**, *122*, 11288–11299.

(34) Tinnin, J.; Bhandari, S.; Zhang, P.; Aksu, H.; Maiti, B.; Geva, E.; Dunietz, B. D.; Sun, X.; Cheung, M. S. Molecular-Level Exploration of the Structure-Function Relations Underlying Interfacial Charge Transfer in the Subphthalocyanine/C_{60} Organic Photovoltaic System. *Phys. Rev. Applied* **2020**, *13*, 054075.

(35) Tinnin, J.; Bhandari, S.; Zhang, P.; Geva, E.; Dunietz, B. D.; Sun, X.; Cheung, M. S. Correlating Interfacial Charge Transfer Rates with Interfacial Molecular Structure in the Tetraphenyldibenzoperiflanthene/C_{70} Organic Photovoltaic System. *J. Phys. Chem. Lett.* **2022**, *13*, 763–769.

(36) Tinnin, J.; Aksu, H.; Tong, Z.; Zhang, P.; Geva, E.; Dunietz, B. D.; Sun, X.; Cheung, M. S. CTRAMER: An Open-Source Software Package for Correlating Interfacial Charge Transfer Rate Constants with Donor/Acceptor Geometries in Organic Photovoltaic Materials. *J. Chem. Phys.* **2021**, *154*, 214108.

(37) Coalson, R. D.; Evans, D. G.; Nitzan, A. A Nonequilibrium Golden Rule Formula for Electronic State Populations in Nonadiabatically Coupled Systems. *J. Chem. Phys.* **1994**, *101*, 436.

(38) Evans, D. G.; Coalson, R. D. Incorporating Backflow into a Relaxation Theory Treatment of the Dynamics of Nonequilibrium Nonadiabatic Transition Processes. *J. Chem. Phys.* **1995**, *102*, 5658–12.

(39) Evans, D. G.; Coalson, R. D. Simulation of Electron Transfer in Polar Solvents: Effects of Nonequilibrium Initial State Preparation. *J. Chem. Phys.* **1996**, *104*, 3598–12.

(40) Cho, M.; Silbey, R. J. Nonequilibrium Photoinduced Electron Transfer. *J. Chem. Phys.* **1995**, *103*, 595–606.

(41) Izmaylov, A. F.; Mendive Tapia, D.; Bearpark, M. J.; Robb, M. A.; Tully, J. C.; Frisch, M. J. Nonequilibrium Fermi Golden Rule for Electronic Transitions Through Conical Intersections. *J. Chem. Phys.* **2011**, *135*, 234106.

(42) Endicott, J. S.; Joubert-Doriol, L.; Izmaylov, A. F. A Perturbative Formalism for Electronic Transitions through Conical Intersections in a Fully Quadratic Vibronic Model. *J. Chem. Phys.* **2014**, *141*, 034104.

(43) Matyushov, D. V. Nonequilibrium Vibrational Population and Donor-Acceptor Vibrations Affecting Rates of Radiationless Transitions. *J. Chem. Phys.* **2019**, *150*, 074504.

(44) Borrelli, R.; Peluso, A. The Temperature Dependence of Radiationless Transition Rates from Ab Initio Computations. *Phys. Chem. Chem. Phys.* **2011**, *13*, 4420.

(45) Song, K.; Shi, Q. Theoretical Study of Photoinduced Proton Coupled Electron Transfer Reaction Using the Non-perturbative Hierarchical Equations of Motion Method. *J. Chem. Phys.* **2017**, *146*, 184108.

(46) Sun, X.; Geva, E. Nonequilibrium Fermi's Golden Rule Charge Transfer Rates via the Linearized Semiclassical Method. *J. Chem. Theory Comput.* **2016**, *12*, 2926–2941.

(47) Sun, X.; Geva, E. Non-Condon Nonequilibrium Fermi's Golden Rule Rates from the Linearized Semiclassical Method. *J. Chem. Phys.* **2016**, *145*, 064109.

(48) Hu, Z.; Tong, Z.; Cheung, M. S.; Dunietz, B. D.; Geva, E.; Sun, X. Photoinduced Charge Transfer Dynamics in the Carotenoid–Porphyrin–C_{60} Triad via the Linearized Semiclassical Nonequilibrium Fermi's Golden Rule. *J. Phys. Chem. B* **2020**, *124*, 9579–9591.

(49) Brian, D.; Sun, X. Linear-Response and Nonlinear-Response Formulations of the Instantaneous Marcus Theory for Nonequilibrium Photoinduced Charge Transfer. *J. Chem. Theory Comput.* **2021**, *17*, 2065–2079.

(50) Brian, D.; Liu, Z.; Dunietz, B. D.; Geva, E.; Sun, X. Three-State Harmonic Models for Photoinduced Charge Transfer. *J. Chem. Phys.* **2021**, *154*, 174105.

(51) Hu, Z.; Brian, D.; Sun, X. Multi-State Harmonic Models with Globally Shared Bath for Nonadiabatic Dynamics in the Condensed Phase. *J. Chem. Phys.* **2021**, *155*, 124105.

(52) Hu, Z.; Sun, X. All-Atom Nonadiabatic Semiclassical Mapping Dynamics for Photoinduced Charge Transfer of Organic Photovoltaic Molecules in Explicit Solvents. *J. Chem. Theory Comput.* **2022**, *18*, 5819–5836.

(53) Hu, Z.; Liu, Z.; Sun, X. Effects of Heterogeneous Protein Environment on Excitation Energy Transfer Dynamics in the Fenna-Matthews-Olson Complex. *J. Phys. Chem. B* **2022**, *126*, 9271–9287.

(54) Liddell, P. A.; Kuciauskas, D.; Sumida, J. P.; Nash, B.; Nguyen, D.; Moore, A. L.; Moore, T. A.; Gust, D. Photoinduced Charge Separation and Charge Recombination to a Triplet State in a Carotene–Porphyrin–Fullerene Triad. *J. Am. Chem. Soc.* **1997**, *119*, 1400–1405.

(55) Liddell, P. A.; Kodis, G.; Moore, A. L.; Moore, T. A.; Gust, D. Photonic Switching of Photoinduced Electron Transfer in a Dithienylethene–Porphyrin–Fullerene Triad Molecule. *J. Am. Chem. Soc.* **2002**, *124*, 7668–7669.

(56) Rozzi, A. C.; Maria Falke, S.; Spallanzani, N.; Rubio, A.; Molinari, E.; Brida, D.; Maiuri, M.; Cerullo, G.; Schramm, H.; Christoffers, J.; Lienau, C. Quantum Coherence Controls the Charge Separation in a Prototypical Artificial Light–Harvesting System. *Nat. Comm.* **2013**, *4*, 1602–1607.

(57) Carbonera, D.; Di Valentin, M.; Corvaja, C.; Agostini, G.; Giacometti, G.; Liddell, P. A.; Kuciauskas, D.; Moore, A. L.; Moore, T. A.; Gust, D. EPR Investigation of Photoinduced Radical Pair Formation and Decay to a Triple State in a Carotene–Porphyrin–Fullerene Triad. *J. Am. Chem. Soc.* **1998**, *120*, 4398–4405.

(58) Kuciauskas, D.; Liddell, P. A.; Lin, S.; Stone, S. G.; Moore, A. L.; Moore, T. A.; Gust, D. Photoinduced Electron Transfer in Carotenoporphyrin–Fullerene Triads: Temperature and Solvent Effects. *J. Phys. Chem. B* **2000**, *104*, 4307–4321.

(59) Gust, D.; Moore, T. A.; Moore, A. L. Mimicking Photosynthetic Solar Energy Transduction. *Acc. Chem. Res.* **2001**, *34*, 40–48.

(60) Spallanzani, N.; Rozzi, C. A.; Varsano, D.; Baruah, T.; Pederson, M. R.; Manghi, F.; Rubio, A. Photoexcitation of a Light-Harvesting Supramolecular Triad: A Time-Dependent DFT Study. *J. Phys. Chem. B* **2009**, *113*, 5345–5349.

(61) Kandrashkin, Y. E. Influence of Spin Decoherence on the Yield of Photodriven Quantum Teleportation in Molecular Triads. *J. Phys. Chem. Lett.* **2021**, *12*, 6405–6410.

(62) Bahr, J. L.; Kuciauskas, D.; Liddell, P. A.; Moore, A. L.; Moore, T. A.; Gust, D. Driving Force and Electronic Coupling Effects on Photoinduced Electron Transfer in a Fullerene-based Molecular Triad. *Photochem. Photobiol.* **2000**, *72*, 598.

(63) Winters, M. U.; Dahlstedt, E.; Blades, H. E.; Wilson, C. J.; Frampton, M. J.; Anderson, H. L.; Albinsson, B. Probing the Efficiency of Electron Transfer through Porphyrin-Based Molecular Wires. *J. Am. Chem. Soc.* **2007**, *129*, 4291–4297.

(64) Brian, D.; Sun, X. Charge-Transfer Landscape Manifesting the Structure-Rate Relationship in the Condensed Phase via Machine Learning. *J. Phys. Chem. B* **2021**, *125*, 13267–13278.

(65) Lai, Y.; Geva, E. On Simulating the Dynamics of Electronic Populations and Coherences via

Quantum Master Equations Based on Treating Off-Diagonal Electronic Coupling Terms as a Small Perturbation. *J. Chem. Phys.* **2021**, *155*, 204101.

(66) Feynman, R. P.; Hibbs, A. R. *Quantum Mechanics and Path Integrals*; McGraw-Hill: New York, 1965.

(67) Tuckerman, M. E. *Statistical Mechanics: Theory and Molecular Simulation*; Oxford University Press: New York, 2010.

(68) Voityuk, A. A.; Rösch, N. Fragment Charge Difference Method for Estimating Donor–Acceptor Electronic Coupling: Application to DNA π-Stacks. *J. Chem. Phys.* **2002**, *117*, 5607–5616.

(69) Meyer, H.-D.; Miller, W. H. A Classical Analog for Electronic Degrees of Freedom in Nonadiabatic Collision Processes. *J. Chem. Phys.* **1979**, *70*, 3214–3223.

(70) Stock, G.; Thoss, M. Semiclassical Description of Nonadiabatic Quantum Dynamics. *Phys. Rev. Lett.* **1997**, *78*, 578–581.

(71) Cotton, S. J.; Miller, W. H. Symmetrical Windowing for Quantum States in Quasi-Classical Trajectory Simulations: Application to Electronically Non-Adiabatic Processes. *J. Chem. Phys.* **2013**, *139*, 234112.

(72) Cotton, S. J.; Igumenshchev, K.; Miller, W. H. Symmetrical Windowing for Quantum States in Quasi-Classical Trajectory Simulations: Application to Electron Transfer. *J. Chem. Phys.* **2014**, *141*, 084104.

(73) Miller, W. H.; Cotton, S. J. Communication: Wigner Functions in Action-Angle Variables, Bohr-Sommerfeld Quantization, the Heisenberg Correspondence Principle, and a Aymmetrical Quasi-Classical Approach to the Full Electronic Density Matrix. *J. Chem. Phys.* **2016**, *145*, 081102.

(74) Cotton, S. J.; Miller, W. H. A New Symmetrical Quasi-Classical Model for Electronically Non-Adiabatic Processes: Application to the Case of Weak Non-Adiabatic Coupling. *J. Chem. Phys.* **2016**, *145*, 144108.

(75) Cotton, S. J.; Liang, R.; Miller, W. H. On the Adiabatic Representation of Meyer-Miller Electronic-Nuclear Dynamics. *J. Chem. Phys.* **2017**, *147*, 064112.

(76) Cotton, S. J.; Miller, W. H. A Symmetrical Quasi-Classical Windowing Model for the Molecular Dynamics Treatment of Non-Adiabatic Processes Involving Many Electronic States. *J. Chem. Phys.* **2019**, *150*, 104101.

(77) Mulvihill, E.; Schubert, A.; Sun, X.; Dunietz, B. D.; Geva, E. A Modified Approach for Simulating Electronically Nonadiabatic Dynamics via the Generalized Quantum Master Equation. *J. Chem. Phys.* **2019**, *150*, 034101.

(78) Gao, X.; Saller, M. A. C.; Liu, Y.; Kelly, A.; Richardson, J. O.; Geva, E. Benchmarking Quasiclassical Mapping Hamiltonian Methods for Simulating Electronically Nonadiabatic Molecular Dynamics. *J. Chem. Theory Comput.* **2020**, *16*, 2883–2895.

(79) Saller, M. A. C.; Kelly, A.; Richardson, J. O. On the Identity of the Identity Operator in Nonadiabatic Linearized Semiclassical Dynamics. *J. Chem. Phys.* **2019**, *150*, 071101.

(80) Deng, Y.; Peng, F.; Lu, Y.; Zhu, X.; Jin, W.; Qiu, J.; Dong, J.; Hao, Y.; Di, D.; Gao, Y.; Sun, T.; Zhang, M.; Liu, F.; Wang, L.; Ying, L.; Huang, F.; Jin, Y. Solution-Processed Green and Blue Quantum-Dot Light-Emitting Diodes with Eliminated Charge Leakage. *Nat. Photon.* **2022**, *16*, 505–511.

(81) Dimitriev, O. P. Dynamics of Excitons in Conjugated Molecules and Organic Semiconductor Systems. *Chem. Rev.* **2022**, *122*, 8487–8593.

(82) Strelnikov, A. A.; Konev, A. S.; Levin, O. V.; Khlebnikov, A. F.; Iwasaki, A.; Yamanouchi, K.;

Tkachenko, N. V. Switching Competition between Electron and Energy Transfers in Porphyrin–Fullerene Dyads. *J. Phys. Chem. B* **2020**, *124*, 10899–10912.

(83) Wang, T.; Su, X.; Zhang, X.; Nie, X.; Huang, L.; Zhang, X.; Sun, X.; Luo, Y.; Zhang, G. Aggregation-Induced Dual-Phosphorescence from Organic Molecules for Nondoped Light-Emitting Diodes. *Adv. Mater.* **2019**, *44*, 1904273–7.

(84) Yang, Q.; Hu, Z.; Zhu, S.; Ma, R.; Ma, H.; Ma, Z.; Wan, H.; Zhu, T.; Jiang, Z.; Liu, W.; Jiao, L.; Sun, H.; Liang, Y.; Dai, H. Donor Engineering for NIR-II Molecular Fluorophores with Enhanced Fluorescent Performance. *J. Am. Chem. Soc.* **2018**, *140*, 1715–1724.

(85) Zhang, G.; Zhao, J.; Chow, P. C. Y.; Jiang, K.; Zhang, J.; Zhu, Z.; Zhang, J.; Huang, F.; Yan, H. Nonfullerene Acceptor Molecules for Bulk Heterojunction Organic Solar Cells. *Chem. Rev.* **2018**, *118*, 3447–3507.

(86) Wang, J.; Zheng, Z.; Zu, Y.; Wang, Y.; Liu, X.; Zhang, S.; Zhang, M.; Hou, J. A Tandem Organic Photovoltaic Cell with 19.6% Efficiency Enabled by Light Distribution Control. *Adv. Mater.* **2021**, 2102787.

(87) Li, Y.; Huang, X.; Ding, K.; Sheriff, H. K. M.; Ye, L.; Liu, H.; Li, C.-Z.; Ade, H.; Forrest, S. R. Non-Fullerene Acceptor Organic Photovoltaics with Intrinsic Operational Lifetimes over 30 Years. *Nat. Commun.* **2021**, *12*, 5419.

(88) Shi, Y.; Chang, Y.; Lu, K.; Chen, Z.; Zhang, J.; Yan, Y.; Qiu, D.; Liu, Y.; Adil, M. A.; Ma, W.; Hao, X.; Zhu, L.; Wei, Z. Small Reorganization Energy Acceptors Enable Low Energy Losses in Non-Fullerene Organic Solar Cells. *Nat. Commun.* **2022**, *13*, 3256.

(89) Scholes, G. D.; Fleming, G. R.; Chen, L. X.; Aspuru-Guzik, A.; Buchleitner, A.; Coker, D. F.; Engel, G. S.; van Grondelle, R.; Ishizaki, A.; Jonas, D. M.; Lundeen, J. S.; McCusker, J. K.; Mukamel, S.; Ogilvie, J. P.; Olaya-Castro, A.; Ratner, M. A.; Spano, F. C.; Whaley, K. B.; Zhu, X. Using Coherence to Enhance Function in Chemical and Biophysical Systems. *Nature* **2017**, *543*, 647–656.

(90) Liang, R.; Yu, J. K.; Meisner, J.; Liu, F.; Martinez, T. J. Electrostatic Control of Photoisomerization in Channelrhodopsin 2. *J. Am. Chem. Soc.* **2021**, *143*, 5425–5437.

(91) Kim, J.; Nguyen-Phan, T. C.; Gardiner, A. T.; Cogdell, R. J.; Scholes, G. D.; Cho, M. Low-Frequency Vibronic Mixing Modulates the Excitation Energy Flow in Bacterial Light-Harvesting Complex II. *J. Phys. Chem. Lett.* **2021**, *12*, 6292–6298.

TOC Graphic